Exploring the micro-mechanics of drained instability in granular materials

Exploring the micro-mechanics of triaxial instability in granular materials

J. C. Lopera Perez[1], C. Y. Kwok[1], C. O'Sullivan[2], *X. Huang[3] & K. J. Hanley[4]

[1]*Department of Civil Engineering, The University of Hong Kong, Haking Wong Building, Pokfulam Road, Hong Kong*

[2]*Department of Civil and Environmental Engineering, Imperial College London, Skempton Building, London SW7 2AZ, UK*

[3]*Department of Geotechnical Engineering, Tongji University, Yantu Building, 1239 Siping Road, Shanghai, 200092, China*

[4]*Institute for Infrastructure and Environment, School of Engineering, The University of Edinburgh, Edinburgh EH9 3JL, Scotland, UK*

Abstract

The instability of granular materials due to water infiltration under fully drained conditions has been previously considered in experimental studies. While laboratory experiments can provide macro-scale insight into drained instability, the micro-mechanics under such conditions are yet to be explored. This study has employed the Discrete Element Method (DEM) to simulate constant shear drained (CSD) tests for an ideal soil. CSD tests were initiated from a range of packing densities and stress conditions. The DEM simulations were able to qualitatively replicate laboratory CSD tests. The choice of the loading control parameter was seen to play a central role in the macro-scale second-order work to identify an effective failure. All samples considered attained an onset of instability that coincided with fluctuations in the second-order work from a particle scale. The time of occurrence of the onset of instability was seen to depend on initial packing density and stress state. A change in the evolution of macro- and micro-mechanical quantities, showing either a sharp increase or decrease, was observed once the CSD conditions had been reached. Finally, conventional drained then constant volume (CDCV) tests were carried out where the appearance of instabilities and the evolution of macro and micro quantities were found to be different from those observed in CSD tests. The results presented in this study indicate that the constant shear drained loading conditions can result in more unfavourable situations than for undrained loading condition.

Keywords: Discrete-element modelling; fabric/structure of soils; particle-scale behaviour

* Formerly Department of Civil Engineering, The University of Hong Kong and Department of Civil and Environmental Engineering, Imperial College London.

1. Introduction

The possibility of collapse of a granular soil under static and fully-drained conditions was first noticed by Lindenberg and Koning (1981). Later it was shown that water infiltration under saturated drained conditions could trigger the failure of geotechnical structures such as slopes which could also be the cause of debris flow (Eckersley, 1990; Olson et al, 2000). In order to investigate this kind of instability, stress-controlled constant shear drained (CSD) triaxial tests have been employed to mimic the infiltration of water and the stress state in a slope (e.g. Sasitharam et al (1993)).

In CSD tests, instability is considered to be the rapid development of large plastic strains as the soil becomes unable to sustain the imposed stress (Sawicki and Swidzinski, 2010; Chu et al, 2012). The onset of instability under drained conditions coincides with an increase of strain rate, developing large strains that cause the sample to become uncontrollable (Nova, 1994). Most of the research that has been carried out in this subject consists of laboratory tests (Sasitharam et al, 1993; Anderson and Riemer, 1995; Zhu and Anderson, 1998; Gajo et al, 2000; Chu et al 2003; Chu et al 2012). Several constitutive models that can successfully simulate the instability observed in CSD tests have also been proposed (Darve et al 2004; Sawicki and Swidzinski, 2010; Ramos et al 2012).

Hill's condition of stability (Hill, 1958) has proven to be useful for identifying the onset of instability in CSD tests (Darve et al, 2004; Darve et al, 2007; Sibille et al, 2007; Daouadji, 2010; Nicot et al, 2011; Hadda et al, 2013). Instability and collapse of granular soils under CSD conditions can happen to both loose and dense samples either in a dry or a saturated state (Skopek et al, 1994; Chu et al 2003). This differs markedly from undrained conditions, under which instability is mainly observed in saturated loose to medium dense samples. Undrained tests are usually carried out under strain-controlled conditions, where the onset of instability is correlated with an initial peak in deviator stress, according to the concept of collapse surface introduced by Sladen et al. (1985). The relationship between the state parameter (as proposed by Been and Jefferies (1985)) and the stress ratio at the onset of instability for undrained tests can also serve as an indicator of instability for CSD tests (Chu et al 2003; Chu et al 2012). For conventional undrained tests this relationship is bound by a critical density that marks the limit at which samples can attain an unstable behaviour (Lindenberg and Koning, 1981).

While extensive information from a macro scale has been reported for CSD tests, the micro-mechanics of the onset of instability and subsequent collapse for these stress conditions are yet to be explored. Moreover, the underlying mechanism that accounts for drained and undrained instabilities remains unclear. Ning et al. (2013) showed that the discrete element method (DEM) (Cundall and

Strack, 1979) can act as a tool to simulate CSD tests. This contribution aims to fill these gaps by conducting DEM tests to simulate the instability behaviour of an ideal granular soil.

2. DEM Simulations

This study used a modified version of the open-source code LAMMPS (Plimpton, 1995). As shown in Figure 1, three-dimensional numerical samples consisting of 22,312 initially non-contacting spherical particles were created as a representative volume element, enclosed within a cuboidal periodic cell to avoid boundary effects (Thornton, 2000; Huang *et al*, 2014). The stresses in the periodic cell were determined from the stress tensor defined as $\bar{\sigma}_{ij}=\frac{1}{V}\sum_{1}^{N_c} l_i^c f_j^c$, where $\bar{\sigma}_{ij}$ is the stress tensor, V is the volume of the periodic cell, N_c is the total number of contacts, l_i^c and f_j^c are the branch vector and interparticle contact force corresponding to contact c respectively (Bagi, 1996; Potyondy & Cundall, 2004). The particle size distribution (PSD) used for all the simulations is representative of Toyoura sand (Figure 1). A simplified Hertz-Mindlin contact model was used. The input parameters were a particle shear modulus (G) of 29 GPa, a particle Poisson's ratio (ν) of 0.12, a particle density (ρ) of 2650 kg/m^3, and a local damping coefficient of 0.1. A parametric study which compared damping coefficients of 0.01 and 0.1 confirmed that this damping value was low enough to have negligible influence on the observed behaviour. Gravity was inactive during these simulations. All simulations were run on a high-performance cluster using a stable timestep of 5.3 ns. The timestep (δt) for the analyses was calculated as $0.1\sqrt{m/k}$ where m/k is the minimum ratio of particle mass/contact stiffness for the system.

The periodic cell was initially deformed until the system reached an isotropic stress state with an initial mean effective stress (p'_0) of 500 kPa. The system was then subjected to numerical cycling until both p' and the number of contacts became constant, indicating equilibrium. The void ratio of each sample at the end of isotropic compression was controlled using different inter-particle friction coefficients (μ) during the isotropic compression stage. Samples with three different initial densities were considered: dense (e_0 = 0.5533), medium dense (e_0 = 0.6238) and loose (e_0 = 0.6491). For all tests, μ was set to 0.25 after the isotropic compression stage, consistent with values for real quartz particles, where values for μ are in the range of 0.12 – 0.35, as was observed by Senetakis *et al* (2013). The tests carried out included CSD, conventional drained (CD), constant volume (CV) and conventional drained then constant volume (CDCV) tests.

Details of all the tests performed are included in Table 1. In this table, the test notation is divided in four parts, indicating the type of test, p'_0, e_0 and (only for CSD and CDCV) the q at which either the CSD or the constant volume conditions, respectively, were initiated. The strain rate used for the CV

and conventional drained (CD) tests was calculated using the inertial number defined as $I = \dot{\varepsilon} d\sqrt{\rho / p'}$, where $\dot{\varepsilon}$ is the shear rate, d is the mean particle size of the assembly, ρ is the grain density, and p' is the mean effective stress. Maintaining $I \leq$ 2.5e-3, ensures quasi-steady conditions during the shearing process (MiDi, 2004; da Cruz et al, 2005; Lopera et al, 2015).

The two different stress paths considered in this study are shown in Figure 2. In the first case (Figure 2(a)), following isotropic compression, samples were sheared under stress-control drained conditions at constant lateral stresses. As the deviatoric stress (q) reached either 118 kPa or 250 kPa ($q/p' \approx 0.2$ or $q/p' \approx 0.4$), the stress path was changed to CSD, which was achieved with a servo-control by simultaneously reducing the major and minor principal stresses, σ'_1 and σ'_3 respectively, by the same amount. Different stress reduction rates (1 kPa/500 timesteps, 1 kPa/5000 timesteps and 1 kPa/50000 timesteps) were considered, and similar responses were observed. Therefore, only those results for a reduction rate of 1 kPa/5000 timesteps are presented in this paper. The CSD path was continued until the sample lost controllability as defined by Nova (1994). A total of six tests were considered for the first loading path.

In order to find the similarities and differences between the CSD tests and CDCV tests at their different stages, instead of initiating CSD tests upon reaching $q/p' \approx 0.2$, strain-controlled CV tests were performed, i.e., following the second type of loading path presented in Figure 2(b). The loading path just before the start of the CV tests is the same as for the CSD tests. Therefore, differences between the sample responses under CSD and CV conditions can be attributed solely to the different loading conditions.

A third set of tests was performed, consisting of ten conventional CV strain controlled tests, and six conventional drained (CD) tests with constant σ'_3 and strain controlled to obtain the critical state lines in both e-p' and q-p' planes, as well as the stress ratio (at instability state) – state parameter relationship. All these tests used samples that were compressed to an isotropic confining pressure prior to shearing; all of the CV tests had an initial p' of 500 kPa whereas a range of initial p' values between 100 kPa and 5000 kPa were used for the CD tests.

3. Results

3.1 Stress-deformation response

Figure 3 shows how a constant σ'_3 stress path was initially imposed, after which σ'_3 was reduced linearly with time under CSD conditions (stress path shown in Figure 2(a)). Note that in the figures below cross markers indicate the onset of instability for the CSD test, while “plus sign” markers relate the onset of instability for the CDCV test. The instability points were defined by considering the

second-order work at the macro and particle scale together with a criteria involving changes in q and p', as detailed below. After the onset of instability, even though the servo-control algorithm aims to reduce σ'_1 and σ'_3 equally, the sample was not able to sustain a constant deviatoric stress.

Results from six CSD tests in the q-p' plane are plotted in Figure 4. Two CSD tests were carried out for each sample, at q_{CSD} = 118 kPa and q_{CSD} = 250 kPa, where q_{CSD} denotes the deviatoric stress level at which CSD tests were initiated (void ratios at the onset of the CSD tests are included in Table 1). Circular markers indicate the initiation of the CSD tests for q_{CSD} = 118 kPa, while triangular markers indicate the initiation of the CSD tests for q_{CSD} = 250 kPa. The inset figures provide an enlarged view of the CSD stress paths, where a marked decrease in q is observed that finally leads to a loss in controllability and the collapse of the system as described by Nova (1994). This decrease in q appears at a higher p' for looser samples; denser samples follow a longer stress path which crosses the CSL so that decreases in q occur at lower p' values.

The stress paths for two CV tests are also included in Figure 4. The onset of instability for the CV tests (indicated by an initial maximum in q) is marked by the filled stars, and the instability lines (IL), which connect the onset of instability and the origin, are superimposed for two cases with e_0 = 0.6238 and e_0 = 0.6491. Soon after the onset of instability (start of decreases in q) become apparent (Figure 4). Darve et al. (2007), Daouadji et al (2010) and Chu et al. (2012) showed experimentally that CSD tests become unstable as soon as it crosses the instability line defined from a CV test having the same initial density.

A decrease in q for CSD-500-0.6491-118 occurs at almost the same stress ratio as the onset of instability for CV-500-0.6491, agreeing with the observations from Darve et al. (2007), Daouadji et al (2010) and Chu et al. (2012). The test CSD-500-0.6491-250 becomes unstable as soon as CSD conditions are imposed, as it had already crossed the IL before the isotropic unloading. The stress ratios at the which the decrease in q starts for CSD-500-0.6238-118 and CSD-500-0.6238-250 are below that for CV-500-0.6238 in the q-p' plane, suggesting that the test CV-500-0.6238 lost controllability before reaching an initial peak in q, moreover fluctuations around the initial peak in q are noted as well. In fact, the initial peak in q does not indicate an effective failure, given that q is seen to steadily increase again after reaching a minimum in p', becoming dilatant.

The axial strain rate against time is presented in Figure 5(a) for the CSD tests. For all tests, the strain rates are initially lower than 100 s^{-1} but sharply increase approaching the end of the tests. The densest sample experiences very low strain rates (< 1 s^{-1}) that yield a low I (≤ 2.5e-3) indicating quasi-static states (inertial forces are negligible). The increase in strain rate observed at the onset of instability, together with a decrease in p', leads to an increase in I (>1e-3), indicating that the system is moving

179 from the quasi-steady regime into the dense flow regime (da Cruz et al, 2005). In the dense flow
180 regime, the inertial forces become relevant and granular materials start flowing like a liquid (Jop et al,
181 2006). After collapse, the strain rate increases sharply for all samples tested with values ranging from
182 57.24 s^{-1} (I = 0.062) to more than 390.6 s^{-1} (I = 0.4241). An $I > 0.1$ indicates that the system is in the
183 collisional dynamic regime where inertial forces are dominant.
184
185 Figure 5(b) shows the volumetric strain (ε_v) against time for the CSD tests. For dense (e_0=0.5533) and
186 medium dense (e_0=0.6238) samples, dilation takes place throughout the entire test. In contrast, the
187 loose sample (e_0=0.6491) sheared from q_{CSD} = 118 kPa dilates for a short period of time after the CSD
188 reaching a minimum value of ε_v after which the sample contracts. For the loose sample sheared from
189 q_{CSD} = 250 kPa, even though an isotropic unloading is taking place, the sample had already failed and
190 thus immediately became contractant.
191
192 More details of the strain rate and ε_v at small strains are presented in Figures 5(c) and 5(d). The dense
193 and medium dense sample contract initially, followed by an abrupt change to dilation as soon as the
194 CSD conditions are imposed. Although its overall volumetric response is dilative, the dense sample
195 initially extends in the axial strain direction until ε_1 reaches 0.005%, after which the dense sample
196 becomes compressive again in the axial direction. The tendency for ε_1 to reverse diminished with a
197 higher q_{CSD} and with an increase in e_0. Both the dense and medium dense samples with q_{CSD} = 250 kPa
198 showed no reversal in ε_1, while the medium dense sample with q_{CSD} = 118 kPa showed a negligible
199 reversal in ε_1. Similar responses in terms of reversal of ε_1 were found by Darve et al (2004) and Nicot
200 et al (2011). For the loose sample with q_{CSD} = 118 kPa, a short period of dilation took place as soon as
201 CSD conditions were imposed. The sample contracted again at around 0.1% of ε_1 indicating
202 instability, that is, an isotropic unloading is becoming contractant. At small strains, the loose sample
203 with q_{CSD} = 250 kPa did not show either a reversal of ε_1 or a drop in ε_1. Although the inset figure at the
204 bottom of Figure 5(b) shows that the rate in contraction reduces after imposing the isotropic unloading
205 for the loose sample with q_{CSD} = 250, no dilation was present in this sample given that it had already
206 crossed the bifurcation domain boundary when CSD conditions took place.
207
208 Figure 5(a) shows how the sharp increase in strain rate coincides with the onset of instability. In
209 Figure 5(b), collapse, marked by the rapid development of volumetric strain, occurs immediately after
210 the onset of instability for the dense sample. However, for the medium dense and loose samples, a
211 longer period of shearing is required before collapse occurs. The volumetric behavior after collapse is
212 fairly similar in all samples considered, and is always related to a sudden and sharp drop of
213 volumetric strain.
214

Figure 6 presents the macro response of the CDCV tests along with the CSD tests for direct comparison on the *q-p'* stress plane. During constant volume conditions, instability occurs once a local maximum in *q* is reached. As indicated in the *q-p'* stress plane in Figure 6(a), only the loose sample reached instability. Subsequently, it fully liquefied to *p'* = 0 kPa and *q* = 0 kPa. Both the medium dense and dense sample continued to show an increase in *q* with a dilative tendency (increase in *p'* and *q*).

The bottom figure of Figure 6(a) includes the stress path of a CV tests sheared from the same initial void ratio, the instability line (joining the peaks in *q* for the CV test with the origin) and the onsets of instability from the CV, CSD and CDCV tests. The onset of instability from the CDCV tests appears immediately after crossing the instability line and thus the time the CDCV test needed to become unstable is given by the time it took to reach the instability line. This result also suggests that, had the sample been switched to CV conditions after crossing the instability line, no time would have been allowed between imposing the CV conditions and failure. It is shown how the onsets of instability for three different tests are attained closely at the instability line, suggesting that regardless of the kind of test (CV, CSD or CDCV) once the stress path crosses the instability boundary domain an onset of instability will be attained.

Figure 6(b) shows *q* against time. As soon as the CDCV test is initiated, the three samples start to deviate from each other. The dense and medium dense samples show no sign of instability under CDCV conditions. A sharp increase in *q* is observed for the dense sample, which diminishes as e_0 increases. The loose sample under CDCV conditions experienced the onset of instability earlier than the CSD test. By the time that the CSD attained its onset of instability, *q* for the CDCV test is already lower than that for the CSD test. It was shown by Darve et al (2007) how, once the stress path crosses the bifurcation domain boundary, failure would appear immediately. This bifurcation domain boundary corresponds to the instability line from a CV test.

Figure 7(a) shows the *e-p*' response for the CSD tests discussed above. The critical state line obtained from those conventional drained and undrained triaxial tests described in Table 1 is overlaid and is represented by a linear relationship following Li and Wang (1998). In all cases, the onset of instability occurs before reaching the critical state line. At the onset point of collapse, the failure mechanism is dilation regardless of the initial state. For the loose sample (e_0 = 0.6491), it initially contracts towards the critical state line after the onset of instability, and crosses the CSL followed by dilation before collapsing. Similar observations in the *e-p'* plane from laboratory CSD tests have been reported by Chu and Leong (2001).

Been and Jefferies (1985) introduced the concept of the state parameter (ψ), defined as the difference between the initial void ratio before shearing takes place (e_0) and the void ratio at the critical state (e_{cs}) at the same p'. A positive ψ indicates a loose state with a tendency to contract, while a negative ψ indicates a dense state with a tendency to dilate. Figure 7(b) includes data points relating the stress ratio ($\eta = q/p'$) at the onset of instability and the state parameter for the CSD and CV tests (filled diamonds). In general, the data points from the CSD tests can be represented by a linear relationship. Data points corresponding to the onset of instability state for medium dense and loose samples in CSD tests are close to the data points for the CV tests.

Test CSD-500-0.6491-118 and test CV-500-0.6491 have the same e_0 and attain an almost identical relationship between stress ratio at the onset of instability and the initial state parameter. Data points corresponding to CSD tests deviate from the CV $\eta - \psi$ relationship. These tests find their onset of instability at higher η (after crossing the CSL on the q-p' plane, as seen in Figure 4). While laboratory tests have shown that dense samples may also experience unstable behavior under CSD conditions (Chu and Leong, 2001, Ramos et al 2012), it should be noted that for CV cases a $\eta - \psi$ relationship would only be valid up to a certain critical density (Lindenberg and Koning, 1981), beyond which the soil would stop experiencing an onset of instability (in our case e_0= 0.6238). For this reason, data points showing the $\eta - \psi$ relationship at the onset of instability for the dense sample are not captured by the CV test $\eta - \psi$ relationship.

3.2 Identifying the onset of instability

A number of studies (Darve et al, 2004; Darve et al, 2007; Daouadji, 2010; Nicot et al, 2011; Hadda et al, 2013) have shown that the second-order work in terms of the conditions of stability (Hill, 1958) can serve as a good indicator of diffuse instability. Unlike localized instabilities (i.e., shear bands), diffuse instability results in displacement fields where strain patterns cannot be distinguished as in the case of instabilities present in CSD tests (Darve and Roguiez, 1998; Nicot et al, 2011; Ramos et al, 2012).

Hill's condition of instability states that the stress-strain state is stable if the second-order work is strictly positive ($d^2W = d\sigma' \, d\varepsilon > 0$) for all changes in stress and strain (Darve et al. 2004). The second order work for triaxial conditions is given by Equation (1) (Sawicki and Swidzinski, 2010), while Figure 9 shows the second-order work defined here in Equation (1) for the stress paths shown in Figure 3.

$$d^2W = d\varepsilon_v \, dp' + d\varepsilon_q \, dq \quad (1)$$

Imposing a CSD stress path implies $dq = 0$, and $dp' < 0$, thus an unstable state will be associated with ε_v passing through an extremum (Darve et al. 2004). For CV paths, thus an unstable state will be associated with q passing through an extremum.

In this study, in the case of CSD conditions only isotropic loading is imposed, while CV tests are loaded by strain control. These test conditions follow those that are usually used in laboratory experiments (Chu et al. (2012) and Chu et al (2003)). Experiments conducted by Chu et al. (2012) and Chu et al (2003) showed $d\varepsilon_v > 0$ for loose samples and $d\varepsilon_v < 0$ for dense samples both before and after the onset of instability. Both cases were also obtained in this study (Figure 5), implying that d^2W can remain positive during CSD tests even after the system becomes unstable. d^2W is plotted against time for the dense sample with q_{CSD} = 118 kPa in Figure 8 where the observations of the second-order work do not coincide with Hill's stability condition; that is, the system is clearly both unstable and has $d^2W > 0$. On the other hand, the loose sample with q_{CSD} = 118 kPa which experienced an extremum in ε_v has its onset of instability at the minimum value of ε_v leading to the occurrence of negative values of d^2W (as indicated by cross markers in Figure 8(a)) that matches with start of decrease in q.

Darve et al. (2004) showed theoretically, and Daouadji et al, 2010 showed experimentally, that CSD tests and CV tests have the same bifurcation criteria. The peak in q for the CDCV-500-0.6491-118 and the onset of instability for the test CSD-500-0.6491-118 that corresponds to its extrema of ε_v, that are plotted in the *q-p'* plane in Figures 4 and 6(a), are coincident with the instability line from the CV test. As these samples have the same initial density, the DEM data confirm these earlier observations; it also indicates that stress paths such as CDCV have the same bifurcation criteria as CV tests, providing additional support for the observation of Darve et al. (2004).

As e_0 increases, the fluctuations in d^2W become more evident (refer to the loose sample with q_{CSD} = 250 kPa) and the onsets of instability are seen to appear sooner. Referring to Figure 8(b) the dense sample shared under CDCV conditions showing positive values of d^2W throughout the test. Fluctuations between positive and negative values of d^2W are present for the CDCV test sheared from e_0 = 0.6238; these are mostly related with small fluctuations in q. d^2W shows negative values for the loose CDCV test around the onset of instability (maximum in q) followed by a drop in d^2W after 4 ms which is associated with a decay in q.

Hadda et al (2013) proposed the microscopic formulation for the second-order work defined by Equation (2).

$$W_2^p = \sum_{c \in V} df_i^c dl_i^c + \sum_{p \in V} df_i^p dx_i^p \quad (2)$$

Where l^c is the branch vector connecting the centres of contacting particles within the volume V, f^c is the inter-particle contact force, x^p is the coordinates of particle p, and f^p is the resultant force for

particle p. The first term in Equation (2) is the contact-based second-order work, while the second term is the particle-based second-order work.

The second term of Equation (2) is negligible if the system is in equilibrium (Nicot et al (2011), Hadda et al (2013)). However, once particles within the sample move rapidly, the second term of Equation (2) becomes important. An inspection of the second-order work at a particle scale throughout the CSD tests can serve as an appropriate indicator of the onset of instability. Darve et al (2004) found this approach useful when determining the onset of instabilities in DEM simulations of slopes, where the appearance of negative values of the second-order work coincided with instabilities within the slope. Here the appearance of negative values of W_2^p within the sample corresponds to the onset of instability.

Figure 9 presents the second-order work at a particle scale (W_2^p) against time for the six CSD tests conducted. Referring to Figure 5(b), there is no clear maximum in the volumetric strains for the CSD tests with e_0 of 0.5533 or 0.6238 and so for these CSD tests, the onset of instability was identified from the inability of the system to sustain the imposed q by considering dq/dp' calculated between neighbouring data output points as illustrated in Figure 9. The ratio dq/dp' was zero or very small ($\sim 10^{-7}$) before the onset of instability; following a parametric study, a threshold value of dq/dp' of 1e-3 (i.e., $dq/dp' >$ 1e-3) was taken to identify a reduction in q, marking the onset of instability. These points are marked on Figure 4. It is clear that the instability points for tests CSD-2 and CSD-5 do not lie on the instability line for the CV test with e_0 of 0.6238, i.e., using these criteria to identify instability. These data do not conform to the theory proposed by Darve et al. (2004). The lack of agreement may be due to the use of σ'_1 as a stress variation controlled loading rather than a volume variation controlled loading. However the points identified using $dq/dp' >$ 1e-3 are consistent with the appearance of negative values and initiation of fluctuations in W_2^p. Although for the loose sample with q_{CSD} = 118 kPa an extremum in ε_v allowed the recognition of the onset of instability, W_2^p and dq/dp' are also plotted for this case, to illustrate that its onset of instability also coincided with negative values in W_2^p and rise of dq/dp'. As it becomes more difficult for samples to sustain the imposed q, dq/dp' starts to rise and at the same time W_2^p starts to exhibit small-amplitude oscillations around zero. However, once W_2^p becomes negative, dq/dp' shows abrupt and noticeable changes. While the contact-based second-order work ($W_2^p(c)$) decreases consistently to negative values after the initiation of instability, the particle-based component of second-order work ($W_2^p(p)$) oscillates between positive and negative values and this oscillation accounts for the oscillation of the overall second-order work W_2^p. This agrees with Darve et al (2004) who noted that particles with positive W_2^p remain within a system even after instability has taken place.

The response for the loosest sample sheared under CDCV and CSD conditions is included in Figure 10 which considers variations in W_2^p and dq/dp' with time. The response of W_2^p for the CDCV test shows no fluctuations after the onset of instability with almost negligible negative values, in contrast to the CSD test. The very small negative values of W_2^p are associated with fluctuations of dq/dp' between negative and positive values. Conversely, fluctuations of W_2^p between negative and positive values for CSD tests are linked to an increase in $\mathrm{d}q/\mathrm{d}p'$. From Figure 8 and Figure 10 it is evident that the calculated macroscopic and particle-based second-order work are closely related, having changes in sign or fluctuations taking place virtually at the same instant, in agreement with Darve et al (2007).

Figure 11(a) and 11(b) show how the proportions of particles and contacts carrying negative W_2^p change with time for all 6 CSD tests. For all cases, at the onset of CSD conditions, the proportion of particles with negative W_2^p does not exceed 48% and this proportion remains almost constant from the onset of instability until the end of test. However, the proportion of contacts carrying negative W_2^p is dependent on packing density and stress level. When the CSD conditions are imposed and both packing density and stress level increase, a higher proportion of contacts with negative W_2^p are observed. At the onset of instability, the proportion of contacts with negative W_2^p for the dense samples exceeds 60%. For the medium dense and loose samples the proportion of contacts with negative W_2^p is approximately 60% at the onset of instability, with the exception of the loose sample with q_{CSD} = 250 kPa where this proportion reaches 60% at 2 ms which is about the time the specimen crossed its bifurcation domain boundary. Close to the onset of instability there is a change in the slope in the plots illustrated in Figure 11, with the post-instability slopes reducing as packing density increases.

3.3 Micro-mechanical response

In an attempt to understand the physical basis of instability during CSD tests, two particle-scale parameters were analysed: the structural anisotropy (geometrical and mechanical anisotropies) and the coordination number. Satake (1982) defined the fabric tensor as follows:

$$\Phi_{ij} = \frac{1}{N_c}\sum_1^{N_c} n_i n_j \quad (3)$$

where N_c is the total number of contacts and n_i is the unit contact normal. The largest, intermediate and smallest eigenvalues of the fabric tensor are denoted as Φ_1, Φ_2 and Φ_3, respectively. The deviatoric fabric, $\Phi_1 - \Phi_3$, describes the degree of structural anisotropy.

Rothenburg and Bathurst (1989) analytically proved that the stress ratio is related to different sources of anisotropy including geometrical anisotropy ($a_c = 15/2(\Phi_1 - \Phi_3)$), normal contact force anisotropy (a_n) and tangential contact force anisotropy (a_t), of which a_c and a_n are dominant. The definition of a_n

used here follows Rothenburg & Bathurst (1989) and Guo & Zhao (2013), with the average normal contact force tensor being expressed by Equation (4) (where Φ'_{ij} is the deviatoric part of Φ_{ij}) and its probability distribution given by Equation (5). a_n is related to the second invariant of $a_{ij}^n = (15/2)F_{ij}^{'n}/\bar{f}^0$ as $a_n = \sqrt{(3/2)a_{ij}^n a_{ij}^n}$, where $\bar{f}^0 = F_{ii}^n$ is the average normal contact force calculated considering the entire V, different from the mean normal contact force averaged over all contacts..

$$F_{ij}^n = \frac{1}{4\pi}\int_V \bar{f}_n(V) n_i n_j dV = \frac{1}{N_c}\sum_1^{N_c} \frac{f_n n_i n_j}{1+(15/2)\Phi'_{ij} n_k n_l} \quad (4)$$

$$\bar{f}_n(V) = \bar{f}^0[1+a_{ij}^n] \quad (5)$$

Figure 12(a) and Figure 12(b) plot a_c and a_n against time respectively for the CSD tests shown in Figure 4. The initial a_c is close to zero as all the samples were initiated from an isotropic state. Before the CSD takes place (i.e., during constant σ'_3 shearing), a_c is seen to slowly increase. Once the CSD conditions are imposed, a_c increases sharply. A change in the variation of a_c with time seems to take place around the onset of instability. At the onset of instability, dense samples have attained higher values of a_c than loose samples and after onset of instability and an abrupt increase in a_c occurs which is maintained until collapse. Although q remains virtually constant, a_c does vary during shearing. Even after the onset of instability, a_c continues to increase while q begins to decrease, i.e., contacts continue rearranging towards the loading direction in order to sustain the imposed q value.

Before the initiation of the CSD tests a_n increases linearly. The rate of increase of a_n is clearly affected by the imposition of the CSD stress path. The manner in which a_n increases depends on e_0 and q_{CSD}: dense and medium dense samples with q_{CSD} = 118 kPa show an exponential increase while dense and medium dense samples with q_{CSD} = 250 kPa and both loose samples present a linear increase prior to the onset of instability which rate is affected by e_0. An abrupt drop in a_n is seen closer to the onset of instability as the initial packing density increases, with dense samples showing a larger drop than loose samples. The onset of instability corresponds to a sudden reduction in normal contact force anisotropy, demonstrating that the system is less capable of sustaining the imposed deviatoric load while the system is at the same time losing p'. In conjunction with Figure 13(a) and Figure 13(b), it could be inferred that the overall increase of q/p' post the onset of instability is a consequence of the interplay between a_c and a_n.

The coordination number, defined as $Z = 2N_c/N_p$ where N_p is the number of particles, is shown in Figure 12(c) and Figure 12(d) for the cases of q_{CSD} = 118 kPa and q_{CSD} = 250 kPa respectively. Slightly modified definitions of the coordination number are also considered: the number of contacts that are contributing to W_2^p ($Z_{W_2^p}$) (contacts that remained present after two consecutive data outputs),

427 the number of contacts having positive W_2^p ($Z_{+W_2^p}$) and the number of contacts having negative W_2^p
428 ($Z_{-W_2^p}$). In each case the number of contacts is normalized by the total number of particles in the
429 system. As shearing takes place there is a quick drop in $Z_{+W_2^p}$ together with a sudden increase of
430 $Z_{-W_2^p}$ that results in an almost constant Z. After the CSD conditions have been imposed, $Z_{W_2^p}$ decreases
431 notably at a rate which depends on e_0. At the onset of instability for all cases $Z_{W_2^p}$ and $Z_{-W_2^p}$ appear to
432 be approaching a value of $Z = 4$ leaving $Z_{+W_2^p}$ below $Z = 1$. When collapse starts, a sharper drop in
433 $Z_{W_2^p}$ is observed with values either close to $Z = 4$ or below. $Z_{+W_2^p}$ is seen close to zero at collapse
434 while $Z_{-W_2^p}$ appears closer to $Z = 4$ but still below 4. Fluctuations in Z are also present which start
435 appearing as packing density and stress level increases. Ning et al. (2013) demonstrated an absence of
436 strain localization in their CSD tests by showing the distribution of the coordination number (Z) along
437 a vertical plane. Contour plots of Z on a vertical plane at the onset of instability and at end of test
438 (collapse) for a dense sample (CSD-500-0.5533-250) following a CSD path are given in Figure 13. It
439 is clear that at both stages the specimen shows an effectively homogeneous distribution of the
440 coordination number indicating that the mode of instability is diffuse.
441
442 To illustrate the influence of contact and normal contact force anisotropy for contacts carrying either
443 negative or positive W_2^p Figure 14 presents contact rose diagrams for a dense and a loose sample at the
444 onset of instability with a stress level from q_{CSD} = 250 kPa. The radial length of each bin gives the
445 number of contacts present within the angle defining the bin. The colour of each bin is proportional to
446 the average normal contact force that is oriented in that bin. Regardless of contacts carrying either
447 negative or positive W_2^p, a larger number of contacts being aligned in the vertical direction (major
448 principal stress direction) are observed from the dense and loose sample. Figure 14 also shows that
449 contacts carrying either negative or positive W_2^p present a similar average normal contact force for
450 each direction. However, due to the higher number of contacts with negative W_2^p, at the onset of
451 instability, contacts with negative W_2^p are carrying a larger amount of normal force mostly aligned in
452 the vertical direction. From the onset of instability onwards, q is transmitted mostly by contacts that
453 are doing a negative W_2^p which provokes the overall instability of the system.
454
455 An inspection of the micro-mechanical response from CDCV and CSD tests is shown in Figure 15.
456 Figure 15(a) shows the increasing evolution of a_c regardless of the loading conditions imposed.
457 However, the shape of increase is different for the CDCV and CSD tests with the CSD showing an
458 exponential increase. For the CDCV test, the increase in a_c is more pronounced as the initial packing
459 density increases. Regardless of e_0, a_c is always higher for the CSD test than for the CDCV. For the
460 loose sample sheared under CDCV, at the onset of instability a_c has not changed significantly. When

461 the sample is liquefying there is a sudden increase of a_c which attains higher values than those at the
462 end of the CSD test. The mechanical anisotropy a_n is presented in Figure 15(b). Similarly to a_c, there
463 is an increase of a_n regardless of the loading conditions imposed. However, the CSD tests increase
464 exponentially which does not occur in the CVCD tests. The rate of increase of a_n is also affected by e_0
465 with denser samples showing sharper increases than loose ones. For the dense and medium dense
466 samples sheared under CSD conditions, a_n shows lower values than those seen in the CDCV tests. A
467 fairly similar response of a_n is observed for the loose sample, where slightly higher values of a_n are
468 observed for the CSD test especially at the onset of instability. While a_n at the end of the CSD test
469 shows a sudden drop regardless of initial packing density, a_n for the loose sample sheared under CV
470 conditions increases sharply as liquefaction is taking place within the sample.
471
472 Z is plotted against time in Figure 15(c) where a decay of Z is observed for both CDCV and CSD tests.
473 However, the shape of decay is different for each type of test. Z at the onset of instability for the dense
474 and medium dense samples sheared under CSD is lower than those achieved for the CDCV test. For
475 the loose sample, Z is fairly similar at the onset of instability regardless of the loading conditions
476 imposed. By the end of the test of the loose sample under CDCV conditions, the majority of contacts
477 have been lost as it liquefies. However, as q is still available for the CSD at the end of test, only a
478 small drop in Z is observed.
479
480 Radjai et al (1998) described weak contacts as those that contribute negatively to the deviatoric stress.
481 Following Huang et al (2015), the characteristic normal contact force (f^*) that marks the transition
482 from negative to positive contribution to the overall deviatoric stress was found at each step, and thus
483 the weak contact proportion was obtained throughout the tests. The weak contact proportion is
484 included in Figure 15(d) where for the dense and medium dense tests a change in the response is
485 observed as soon as either CSD or CV conditions are imposed with tests under CSD conditions
486 showing an overall lower weak contact proportion than CDCV. For the loose sample, no clear
487 difference in the weak contact proportion can be appreciated after the change in loading conditions.
488 Regardless of initial packing density, tests under CSD conditions show an abrupt decrease in the
489 proportion of weak contacts once the onset of instability is reached. For the case of the loose CDCV
490 test no difference in the proportion of contacts that are weak is seen at the onset of instability,
491 however at about 7 ms, the CDCV test starts presenting an increase in the weak contact proportion
492 that goes up to 1 when the system has fully liquefied.
493
494 **4. Conclusions**

495 A series of CSD tests with different densities and stress states were simulated. These simulations were
496 supplemented by CV simulations, carried out to obtain the relationship between the state parameter

and stress ratio at the onset of instability. The simulation schedule included CDCV tests in order to compare the responses under CSD and CV loading conditions. Following Darve et al (2004) and Hadda et al (2013), the particle-scale second-order work was employed to identify the onset of instability for the CSD tests.

The macro-response agrees qualitatively with all characteristics of the onset of stability reported by previous published laboratory tests, e.g., an increase in strain rate and the loss of controllability to final collapse. For loose states, it was verified that CSD, CV and CDCV tests have the same bifurcation criterion according to the second-order work. The dense sample was found not to agree strictly with the macro-scale second-order work criterion where the second-order work remained positive before and after the onset of instability. However, the loose samples both at CSD and CDCV loading conditions, were seen to agree with the macro-scale second-order work, becoming unstable at a minimum in volumetric strain and at the peak of q respectively. The second-order work from a particle scale was seen to be useful in capturing the onset of instability for CSD tests that do not attain an extremum in volumetric strain. Regardless of initial density and deviatoric stress, all samples experienced an onset of instability during the CSD tests. By contrast, only the loose sample liquefied under CDCV conditions, with the medium dense and dense sample showing no signs of instability. At the onset of instability a larger proportion of contacts with negative W_2^p was present in all CSD tests, which were seen to carry most of the normal contact forces. When the stress ratio at the onset of instability (η) is plotted against the initial state parameter (ψ), a linear relationship was found for the CSD tests in $\eta - \psi_0$ space, which differs from the $\eta - \psi$ relationship for the CV tests. While the $\eta - \psi$ relationship for the CV tests is useful in determining the conditions of instability for medium dense and loose samples under CSD conditions, it fails to capture the conditions of instability for dense samples under CSD conditions.

The micro-mechanical quantities explored were found to be dependent on loading conditions, and had marked differences before and after the onset of instability. While the structural anisotropy kept increasing regardless of a constant or decaying q, the normal contact force anisotropy was seen to decrease once the onset of instability was reached, which happened together with the decay in q. The overall stress response post the onset of instability was seen to be a consequence of the interplay between a_c and a_n. The micro-mechanical responses of the CSD tests differed from those of the CDCV tests, with CSD tests presenting higher geometrical and mechanical anisotropies at the onset of instability compared to CDCV tests. The rate of change in all micro-quantities studied was not affected by the onset of instability for the CDCV tests and was only at liquefaction that a sudden change was observed. While all samples sheared under CSD conditions showed unstable behavior, only the loose sample liquefied under CDCV conditions, with the medium dense and dense sample

showing no signs of instabilities. Therefore, it is important to note that the constant shear drained loading conditions can result in more unfavorable situations than for undrained loading conditions.

Acknowledgements

This study was supported by The University of Hong Kong SPACE research fund and the Research Grants Council of Hong Kong - General Research Fund (Grant No. 17203614). This research is conducted using the HKU Information Technology Services research computing facilities that are supported in part by the Hong Kong UGC Special Equipment Grant (SEG HKU09).

References

Anderson, S. A., and Riemer, M. F. (1995). Collapse of saturated soil due to reduction in confinement. *J. Geotech. Eng*. 121(2), 216 – 219.

Bagi, K. (1996). Stress and strain in granular assemblies. *Mech. Mater.* 22, 165-177.

Been, K. and Jefferies, M. G. (1985). A state parameter for sands. *Géotechnique* 35(2), 99 – 112.

Chu, J., and Leong, W. K. (2001). Pre-failure strain softening and pre-failure instability of sand: A comparative study. *Géotechnique*, 51(4), 311 – 321.

Chu, J., Leroueil, S., and Leong, W. K. (2003). Unstable behaviour of sand and its implication for slope instability. *Can*. *Geotech*. *J*. 40(5), 873 – 885.

Chu, J., Leong, W. K., Loke W. L. and Wanatowski D. (2012). Instability of loose sand under drained conditions. *J. Geotech. Eng*. 138(2), 207 – 216.

Cundall P. A. and Strack O. D. L. (1979). A discrete numerical model for granular assemblies. *Géotechnique*, 29(1), 47 – 65.

da Cruz F., Emam S., Prochnow M., J. N. Roux and F. Chevoir (2005). Rheophysics of dense granular materials: Discrete simulation of plane shear flows. *Phys. Rev.* E, 72, 021309

Daouadji, A., AlGali, H., Darve, F., and Zeghloul, A. (2010). Instability of granular materials: Experimental evidence of diffuse mode of failure for loose sands. *J. Eng. Mech.* 136(5), 575–588.

Darve, F. and Roguiez X. (1998). Homogeneous bifurcation in soils, in: Adachi, et al. (Eds.), Localization and Bifurcation Theory for Soils and Rocks, Balkema, pp. 43–50.Darve, F., Servant, G.,

Darve F., Servant G., Laouafa F. and Khoa H. D. V. (2004). Failure in geomaterials: Continuous and discrete analyses. *Comput. Methods Appl. Mech. Eng.* 193(27–29), 3057–3085.

Darve, F., Sibille, L., Daouadji, A., and Nicot, F. (2007). Bifurcations in granular media: Macro- and micro-mechanics approaches. *C. R. Mécanique,* 335(9–10), 496–515.

Eckersley, J. D. (1990). Instrumented laboratory flowslides. *Géotechnique*, 40(3), 489–502.

Gajo, A., Piffer, L., and de Polo, F. (2000). Analysis of certain factors affecting the unstable behaviour of saturated loose sand. *Mech. Cohes.-Frict. Mater*, 5(3), 215–237.

568 Guo N. and Zhao J. (2013). The signature of shear-induced anisotropy in granular media. *Comput.*
569 *Geotech.* 47, 1 – 15
570 Hadda N., Nicot F., Bourrier F., Sibille L., Radjai F. and Darve F. (2013). Micromechanical analysis
571 of second order work in granular media. *Granul. Matter.* 15, 221 – 235.
572 Hill, R. (1958). A general theory of uniqueness and stability in elastic- plastic solids. *J. Mech. Phys.*
573 *Solids*, 6(3), 236–249.
574 Huang, X., Hanley, K. J., O'Sullivan, C. and Kwok, C.Y. (2014). Effect of sample size on the
575 response of DEM samples with a realistic grading. *Particuology*, 15, 107-115.
576 Huang, X., O'Sullivan, C., Hanley, K. J. and Kwok, C.Y. (2015). Partition of the contact force
577 network obtained in discrete element simulations of element tests. *Computational Particle Mechanics.*
578 (Under review)
579 Jop, P., Forterre, Y. and Pouliquen O. (2006). A constitutive law for dense granular flows. *Nature*.
580 441 (8), 727 – 730.
581 Li, X. S., and Wang, Y. (1998). Linear representation of steady-state line for sand. *J. Geotech.*
582 *Geoenviron. Eng.* 124(12), 1215–1217.
583 Lindenberg J. and Koning H. L. (1981). Critical density of sand. *Géotechnique* 31(2), 231 – 245.
584 Lopera, P. J. C., Kwok, C.Y., O'Sullivan, C. Huang, X. and.Hanley, K. J. (2015). Assessing the quasi-
585 steady conditions for shearing in granular media within the critical state soil mechanics framework.
586 *Soils Found*, (Accepted).
587 Nova, R. (1994). Controllability of the incremental response of soil specimens subjected to arbitrary
588 loading programs. *J. Mech. Behav. Mater.* 5(2), 193–201.
589 MiDi G. D. R. (2004). On dense granular flows. *Eur. Phys. J E* 14, 341 – 365.
590 Nicot F., Daouadji A., Laouafa F. and Darve F. (2011) Second-order work, kinetic energy and diffuse
591 failure in granular materials. *Granul. Matter.* 13, 19 – 28.
592 Ning Z., Evans M, T. and Andrade J. (2013) Particulate study of drained diffuse instability in granular
593 material. *ASCE Geocongress 2013*, *Geotechnical Special Publication No. 231: Stability and*
594 *Performance of Slopes and Embankments III, San Diego, CA*, pp. 1290-1299.
595 Olson S. M., Stark T. D., Walton W. H., and Castro, G. (2000). 1907 static liquefaction flow failure of
596 the north dike of Wachusett dam. *J. Geotech. Geoenviron. Eng.* 126(12), 1184–1193.
597 Plimpton, S. (1995). Fast parallel algorithms for short-range molecular dynamics. *J. Comput. Phys.*
598 117, 1-19.
599 Potyondy D. O. and Cundall P. A. (2004). A bonded-particle model for rock. *Int J Rock Mech Min.* 41,
600 1329 – 1364.
601 Radjai F., Wolf D. E., Jean M., and Moreau J. (1998). Bimodal character of stress transmission in
602 granular packings. *Physical Review Letters*, 80 No. 1, 61 – 64.
603 Ramos A. M., Andrade J. E. and Lizcano A. (2012). Modelling diffuse instabilities in sands under
604 drained conditions. *Géotechnique* 62(6), 471 – 478.

Rothenburg L. and Bathurst R. J. (1989). Analytical study of induced anisotropy in idealized granular materials. *Géotechnique* 39(4), 601 – 614.

Sasitharan, S., Robertson, P. K., Sego, D. C., and Morgenstern, N. R. (1993). Collapse behavior of sand. *Can. Geotech. J.* 30(4), 569–577.

Satake, M. (1982). Fabric tensor in granular materials. In *Deformation and failure of granular materials* (eds P. A. Vermeer and H. J. Luger), pp. 63-68. Rotterdam: Balkema.

Sawicki, A., and Swidzinski, W. (2010). Modelling of pre-failure instabilities of sand. *Comput. Geotech.* 37(6), 781–788.

Senetakis K., Coop, M.R. and Todisco, M.C. (2013) Tangential load-deflection behaviour at the contacts of soil particles. *Géotechnique Letters*, 3, No.2, 59-66

Sibille, L., Nicot, F., Donze, F., and Darve, F. (2007). Material instability in granular assemblies from fundamentally different models. *Int. J. Numer. Anal. Methods Geomech.* 31(3), 457–481.

Skopek, P., Morgenstern, N. R., Robertson, P. K., and Sego, D. C. (1994). Collapse of dry sand. *Can. Geotech. J.* 31(6), 1003–1008.

Sladen, J. A., D'Hollander, R. D., and Krahn, J. (1985). The liquefaction of sands, a collapse surface approach. *Can. Geotech. J.* 22(4), 564–578.

Thornton, C. (2000). Numerical simulations of deviatoric shear deformation of granular media. *Géotechnique* 50(1), 43-53.

Zhu, J. H., and Anderson, S. A. (1998). Determination of shear strength of Hawaiian residual soil subjected to rainfall-induced landslides. *Géotechnique* 48(1), 73–82.

Notation

a_n	Normal contact force anisotropy.
e	Void ratio
F_{ij}^n	Average normal contact force tensor
$\overline{f}_n(\Omega)$	Probability distribution function of the average normal contact force tensor
f^*	Characteristic normalized normal contact force.
G	Particle shear modulus
I	Inertial number
p'	Mean effective stress
p'_0	Mean effective stress after isotropic compression
q	Deviatoric stress
ε_1	Major principal strain

ε_v	Volumetric strain
μ	Inter-particle friction coefficient
v	Particle Poisson's ratio
ρ	Particle density
Φ_{ij}	Fabric tensor
Φ_1; Φ_2; Φ_3	Major, intermediate and minor eigenvalues of the fabric tensor (Φ_{ij}).
Z	Coordination number
W_2^p; d^2W	Second-order work at a particle scale; second-order work at a macro scale

627

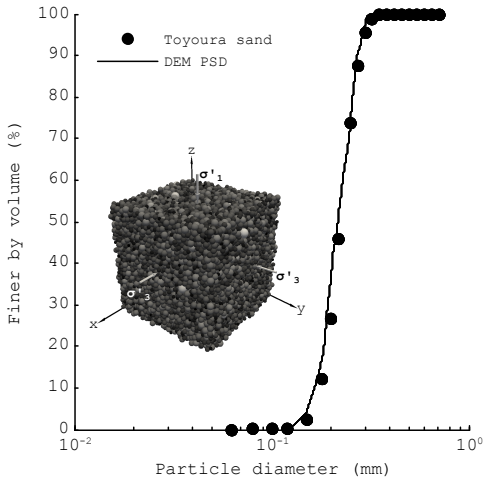

Figure 1. Particle size distribution of numerical samples compared with laboratory data for Toyoura sand. The inset figure shows a representative sample for simulations following isotropic compression.

Figure 2. Stress paths adopted: (a) drained shearing followed by CSD simulation; (b) drained shearing followed by CV simulation.

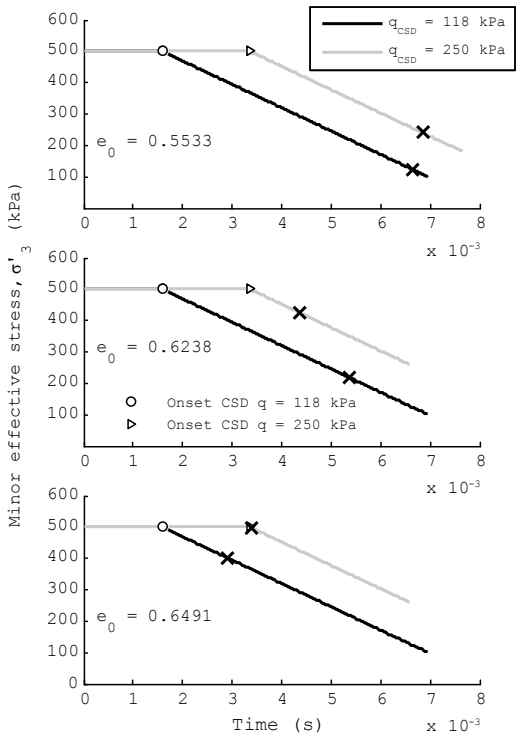

Figure 3. Minor principal effective stress σ'_3 against time. Cross markers indicate the onset of instability for CSD tests. The open circle indicates the onset of CSD conditions for $q_{\mathrm{CSD}} = 118$ kPa, while the open triangle indicates the onset of CSD conditions for $q_{\mathrm{CSD}} = 250$ kPa.

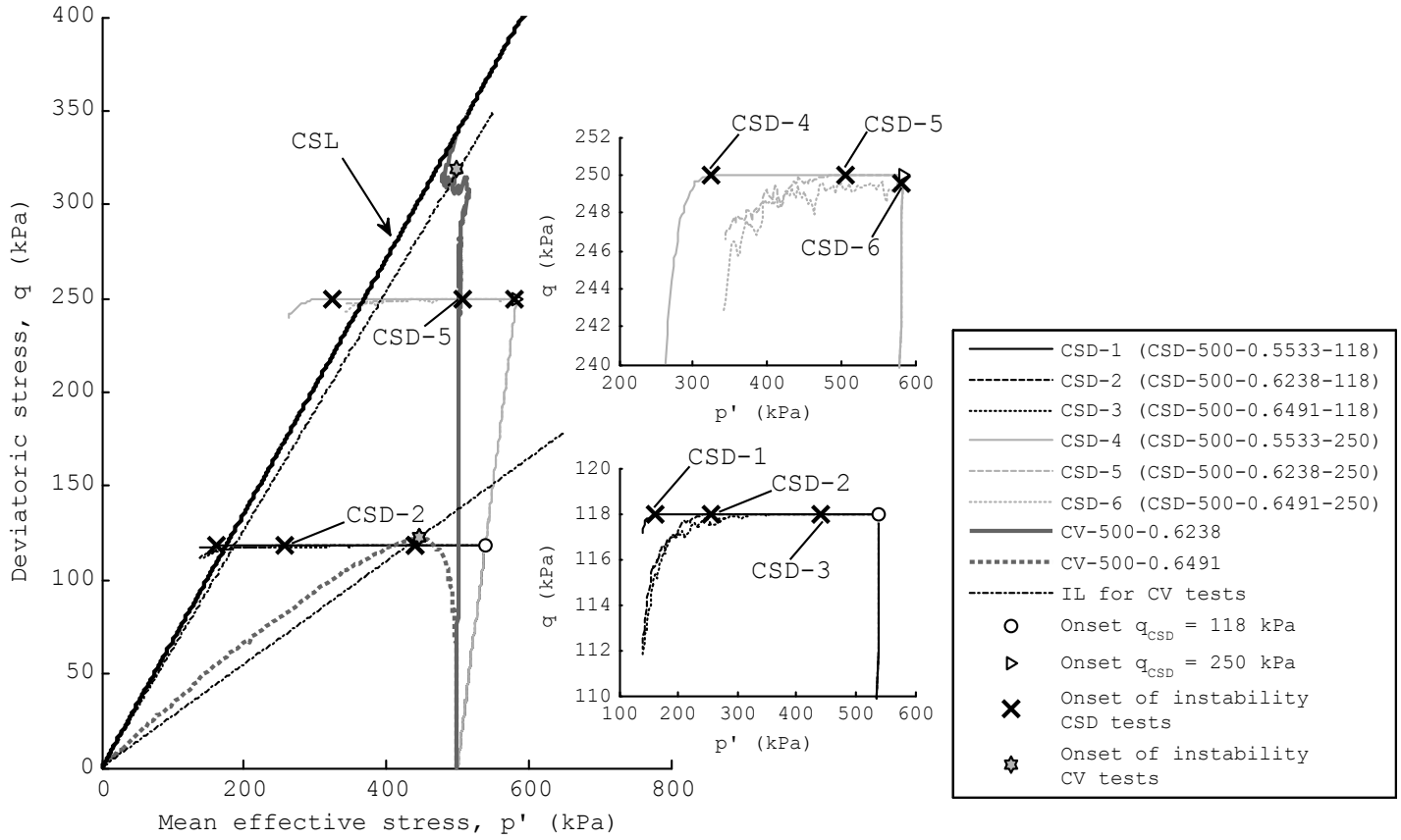

Figure 4. Deviatoric stress q against mean effective stress p' for CSD and CV simulations. Inset figures zoom in to the onset of instability of the CSD tests.

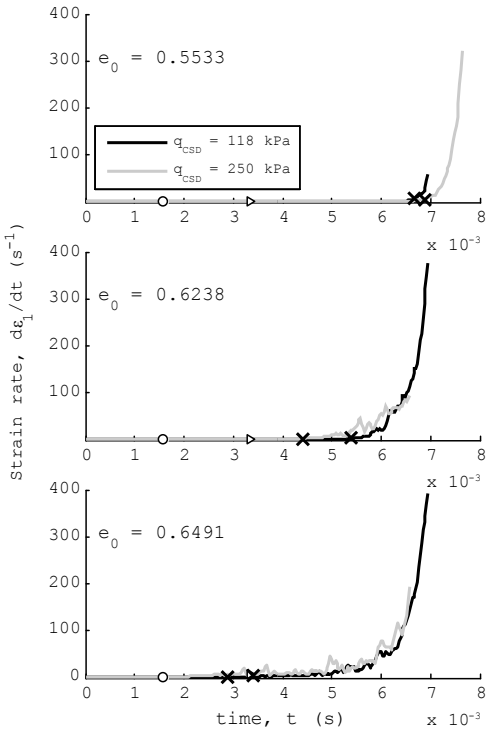

(a)

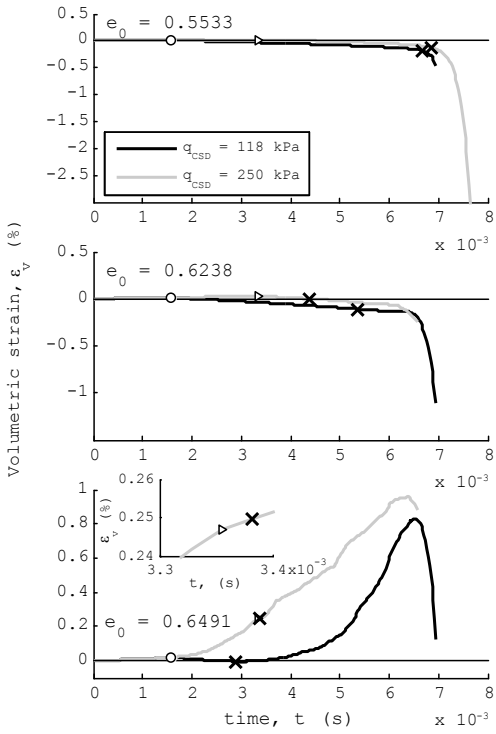

(b)

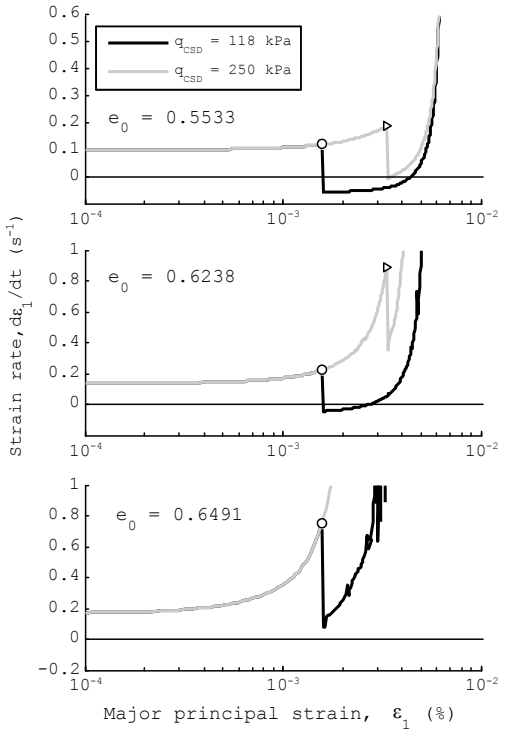

(c)

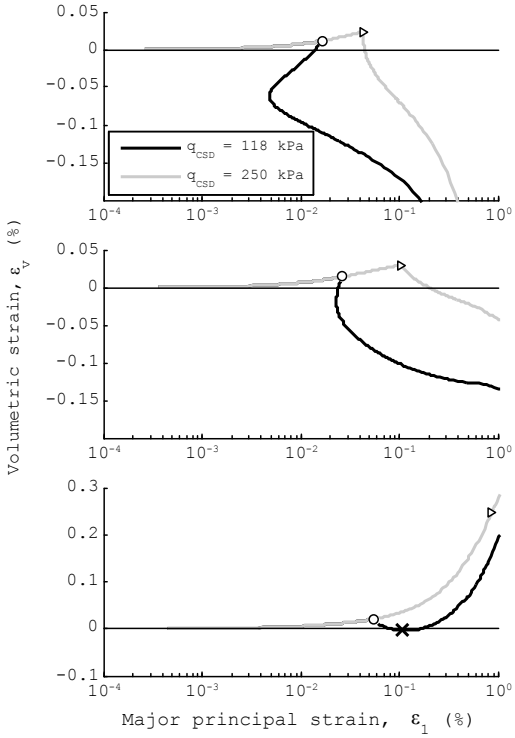

(d)

Figure 5. (a) Strain rate against time, (b) Volumetric strain against time and (c) Strain rate against axial strain for the CSD tests and (d) Volumetric strain against axial strain. Cross markers indicate the onset of instability.

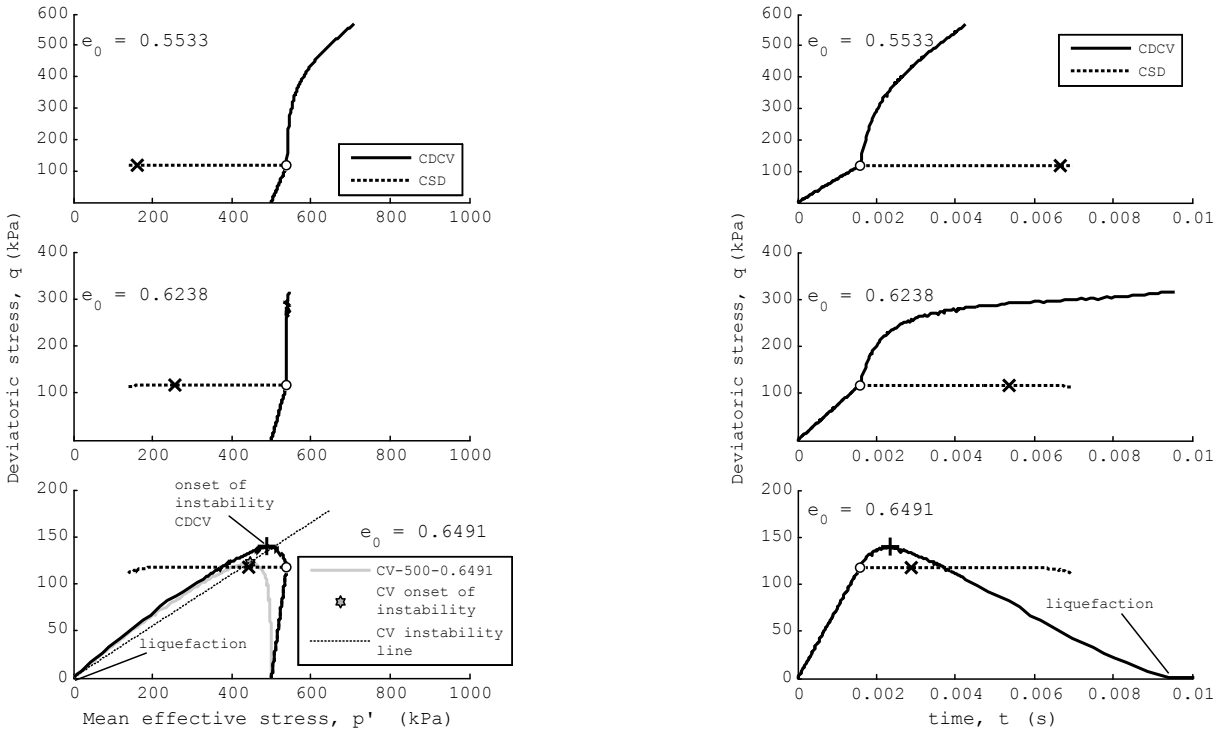

(a) (b)

Figure 6. Comparing the macro-scale responses between CSD test and CDCV tests. (a) q against p'; (b) q against time. Cross markers indicate the onset of instability for CSD tests while plus sign markers indicate the onset of instability for the CDCV test.

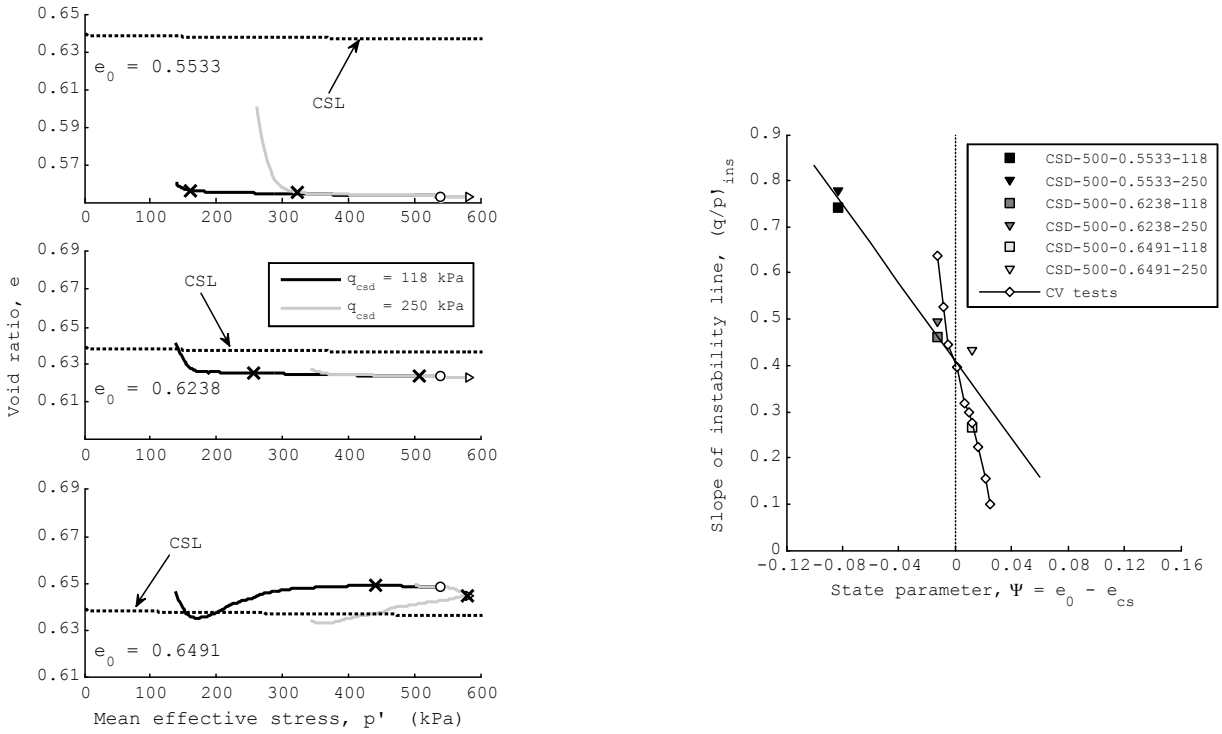

(a) (b)

Figure 7. (a) Void ratio e against mean effective stress p' during CSD shearing; (b) Stress ratio at the onset of instability against state parameter, showing CSD tests and CV tests. Cross markers in Figure 7(a) indicate the onset of instability.

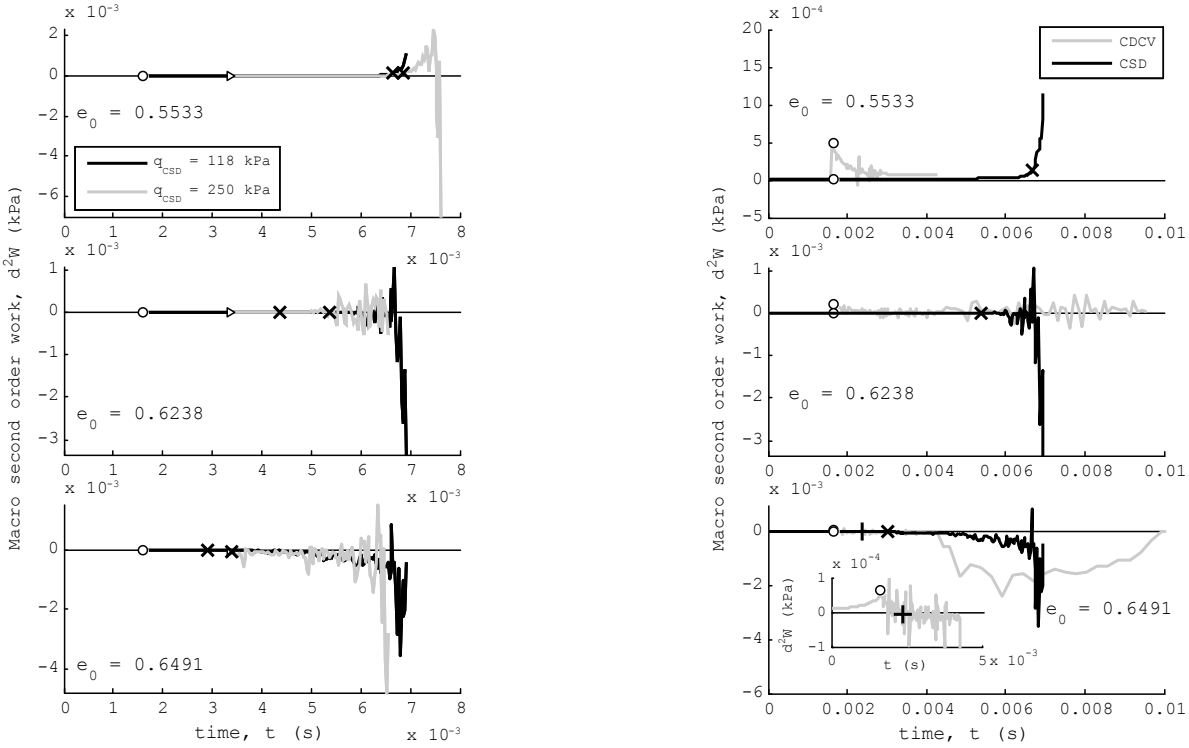

(a) (b)

Figure 8. Macro-scale second-order work against time for (a) all CSD tests and (b) CSD tests with $q_{\mathrm{CSD}} = 118$ kPa and CDCV tests. Cross markers indicate the onset of instability for CSD tests while plus sign markers indicate the onset of instability for the CDCV test

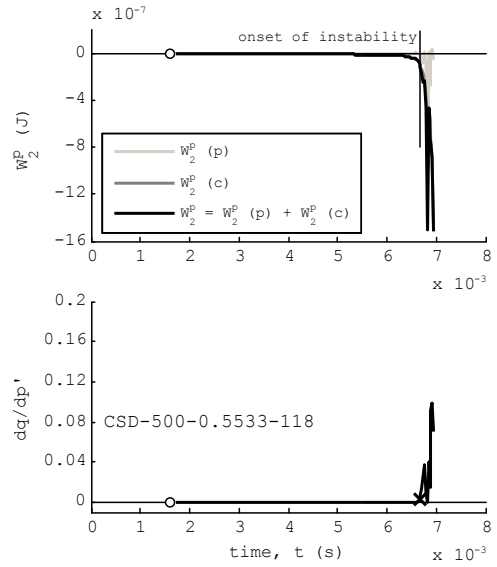

(a)

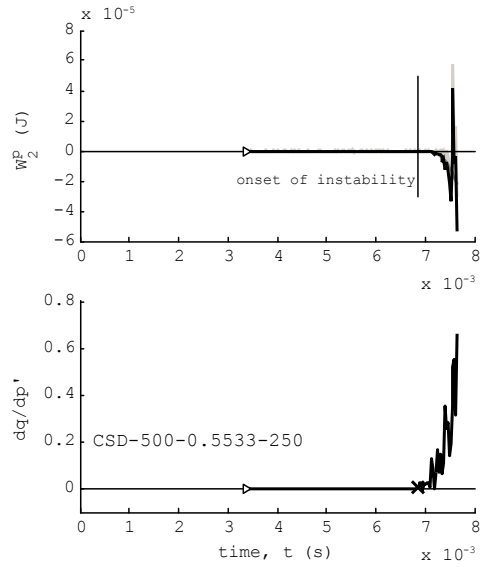

(b)

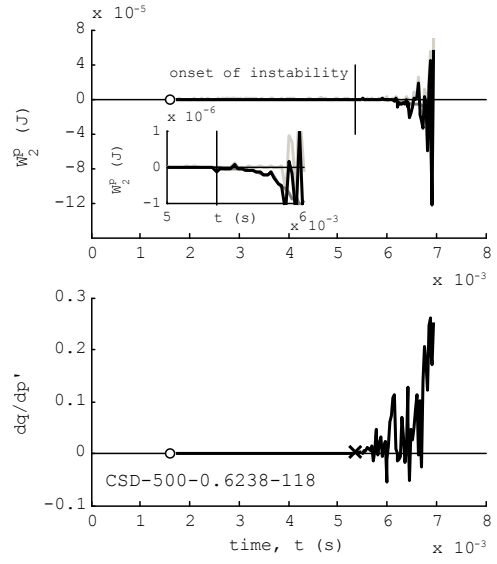

(c)

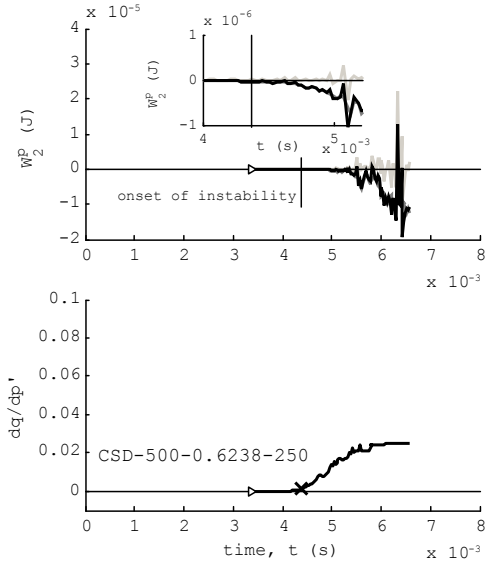

(d)

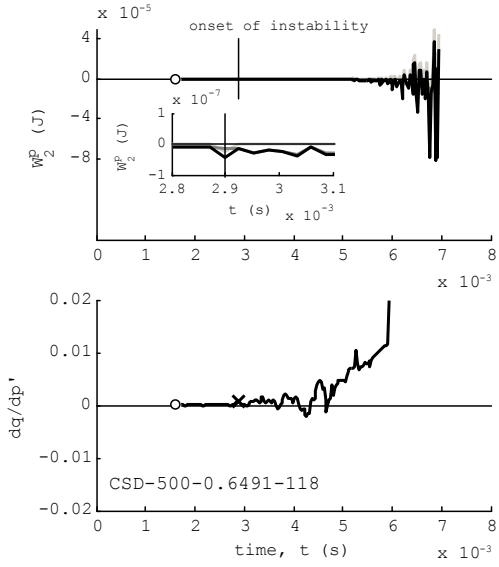

(e)

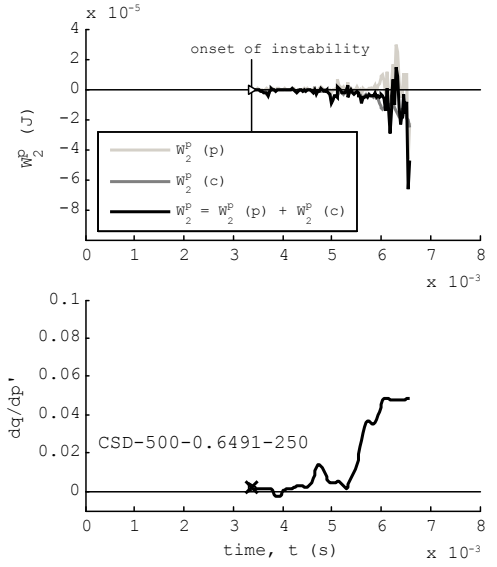

(f)

Figure 9. Micro-scale second-order work and gradient dq/dp' against time for the CSD tests. Cross markers and vertical lines indicate the onset of instability.

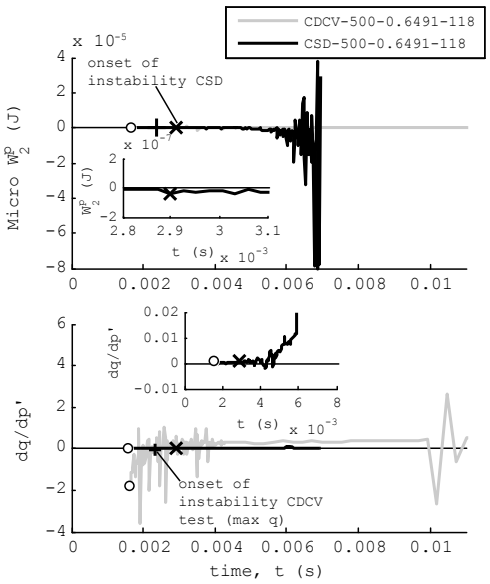

Figure 10. Comparison of micro-scale second-order work and gradient dq/dp' against time between CDCV and CSD tests. Cross markers indicate the onset of instability for CSD tests while plus sign markers indicate the onset of instability for the CDCV test.

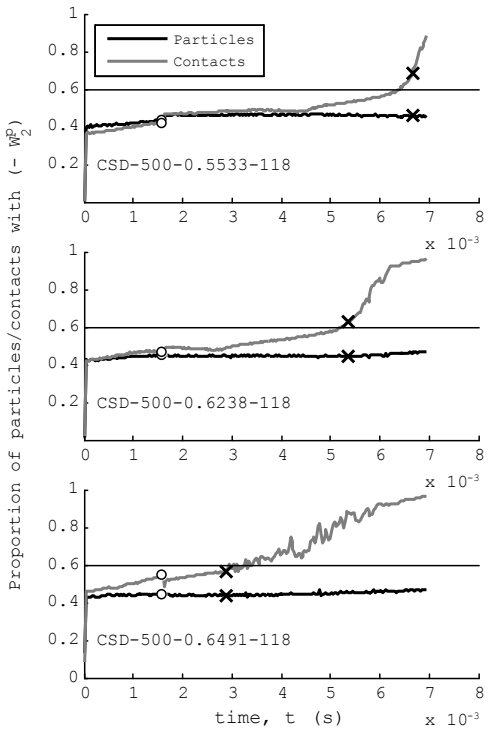

(a)

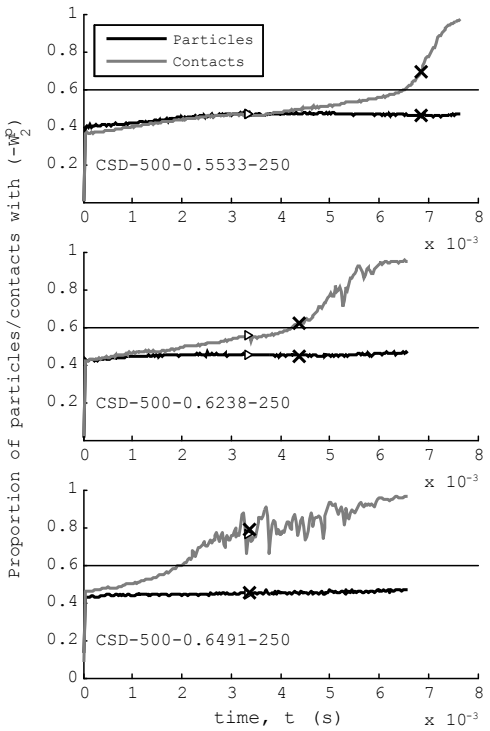

(b)

Figure 11. Proportion of particles and contacts carrying negative micro second order work. (a) $q_{\mathrm{CSD}} = 118$ kPa and (b) $q_{\mathrm{CSD}} = 250$ kPa. Circle and triangle markers indicate the onset of CSD conditions for $q_{\mathrm{CSD}} = 118$ kPa and $q_{\mathrm{CSD}} = 250$ kPa respectively. Cross markers indicate the onset of instability.

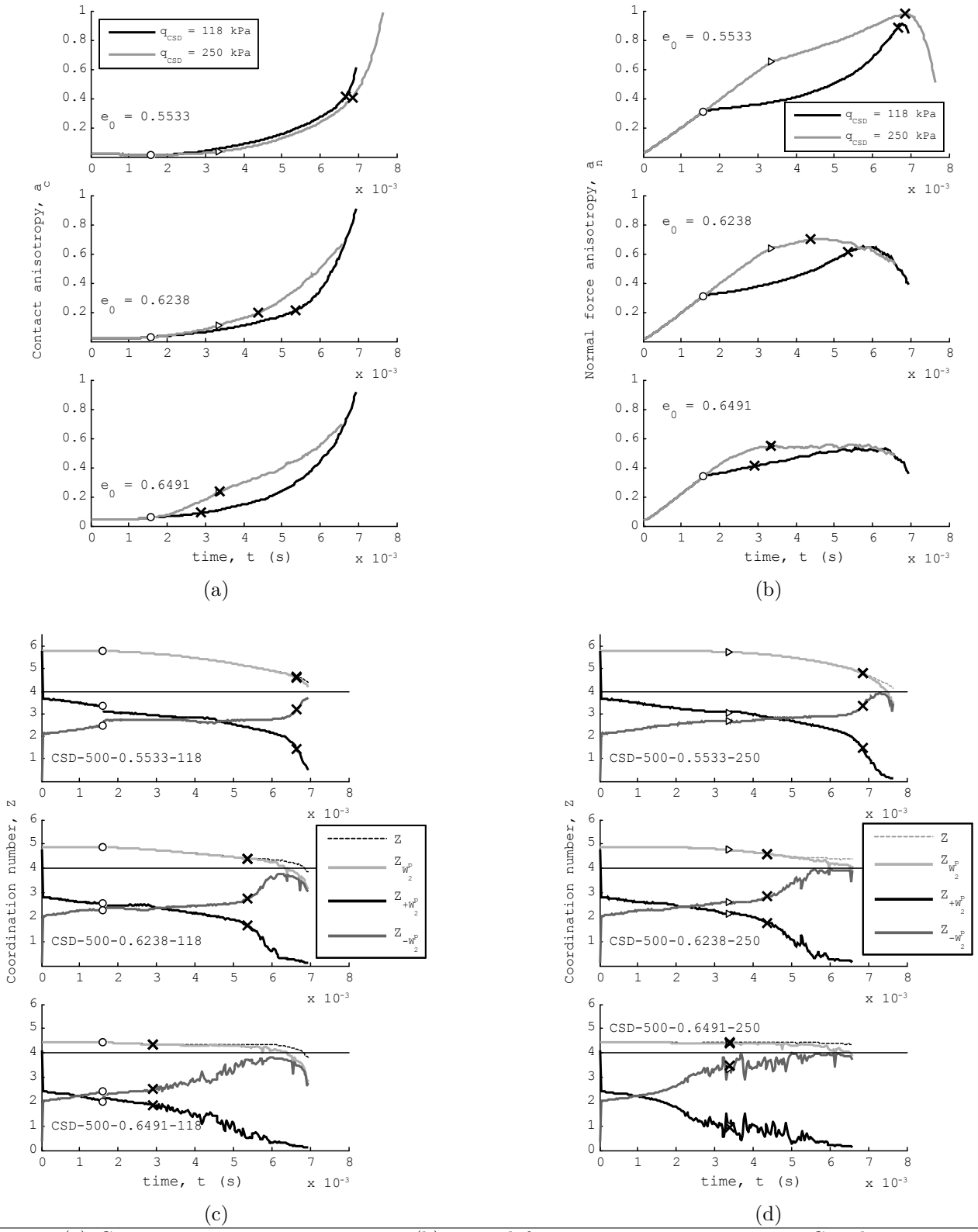

Figure 12. (a) Contact anisotropy against time; (b) normal force anisotropy against time, Coordination number against time for (c) qcsd = 118 kPa and (d) qcsd = 250 kPa. Circle and triangle markers indicate the onset of CSD conditions for $q_{\mathrm{CSD}} = 118$ kPa and $q_{\mathrm{CSD}} = 250$ kPa respectively. Cross markers indicate the onset of instability.

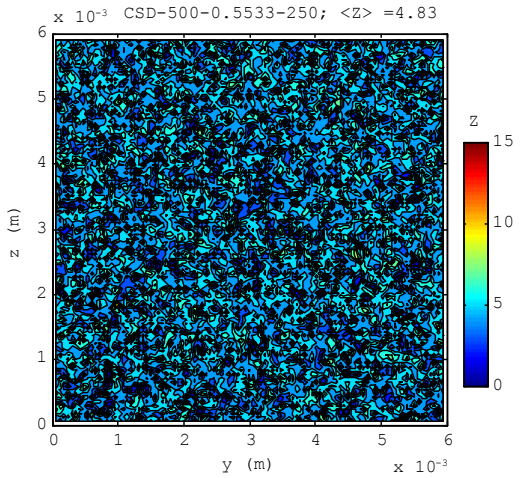

(a)

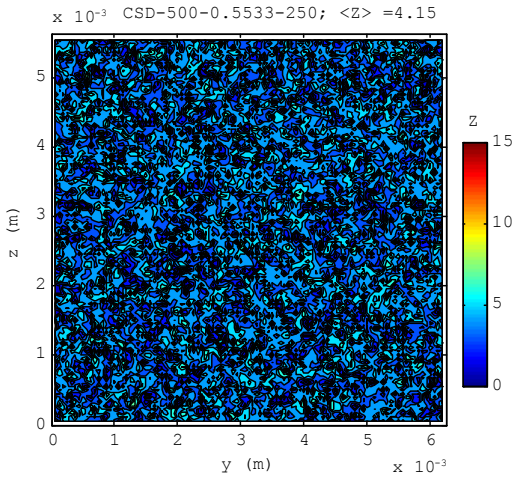

(b)

Figure 13. Contour plots of coordination number across the plane Y-Z for the dense sample CSD-500-0.5533-250. (a) At onset of instability with a mean coordination number ($<Z>$) of 4.83 and (b) at end of test with $<Z> =$ 4.15.

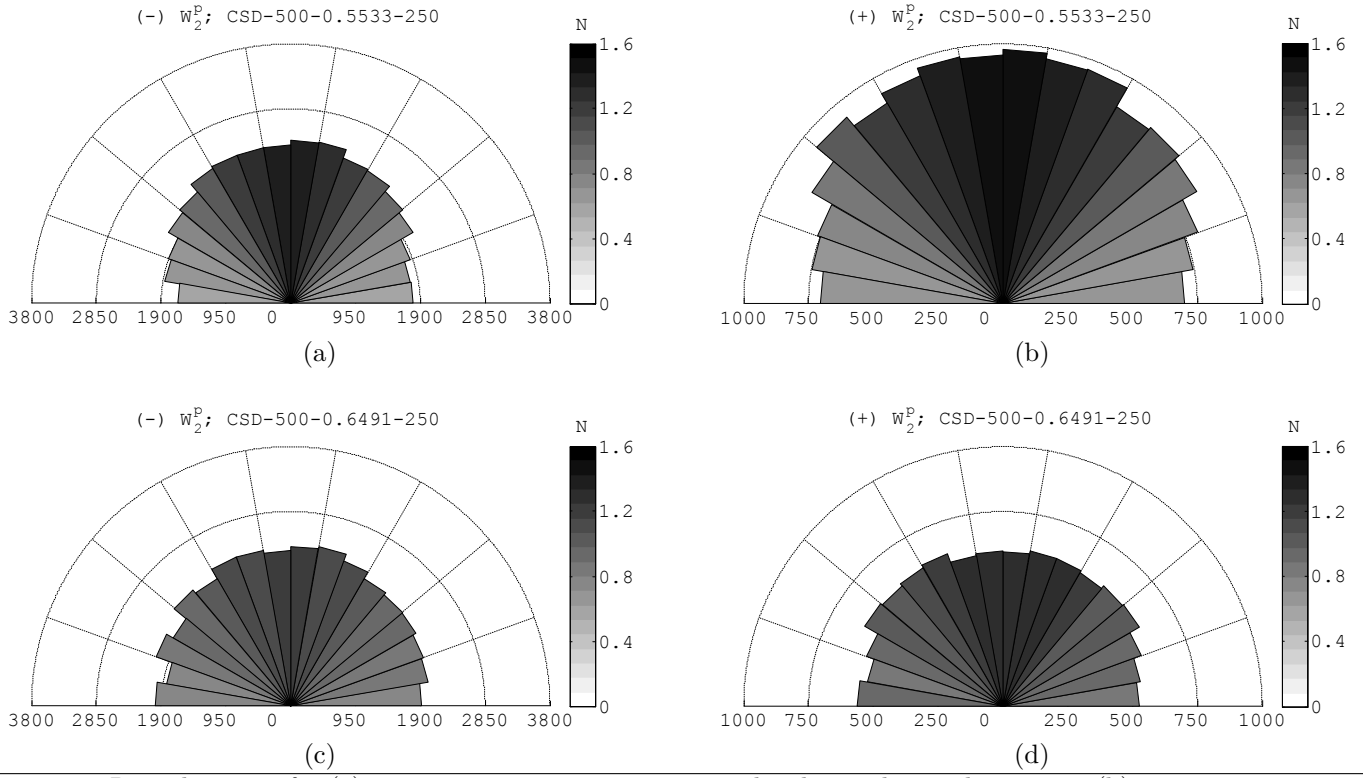

Figure 14. Rose diagrams for (a) contacts carrying negative second order work in a dense state (b) contacts carrying positive second order work in a dense state (c) contacts carrying negative second order work in a loose state and (d) contacts carrying positive second order work in a loose state

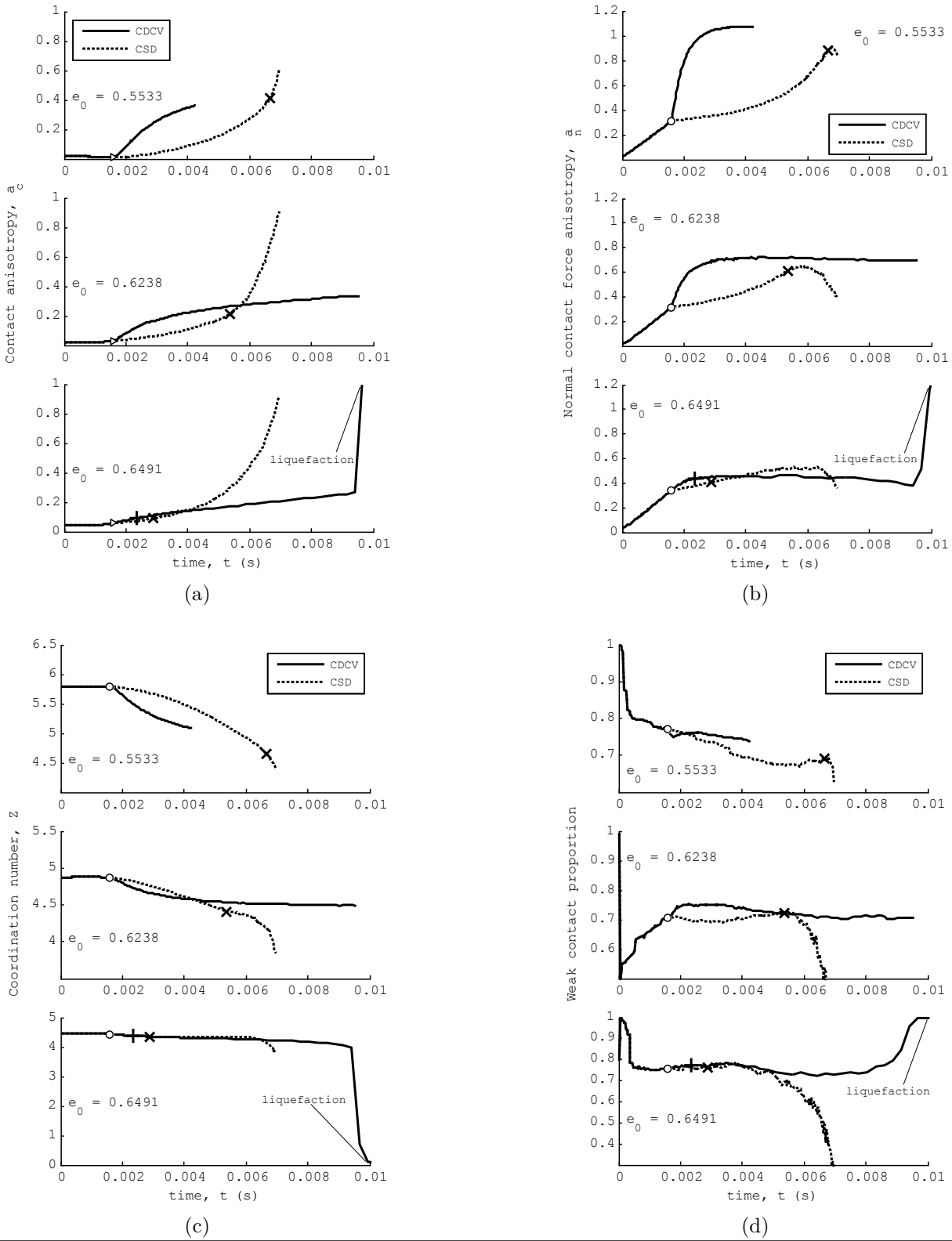

Figure 15. Comparison of the micro response against time for CSD and CDCV tests: (a) Contact anisotropy a_c (b) Normal contact force anisotropy a_n (c) Coordination number (d) Weak contact proportion. Cross markers indicate the onset of instability for CSD tests while plus sign markers indicate the onset of instability for the CDCV test.

Table 1. List of tests conducted

Test ID	e_0	e_{CSD}	p'_0 (kPa)	q_{csd} (kPa)	q_{cv} (kPa)	e_{cs}	p'_{cs} (kPa)	q_{cs} (kPa)
CSD-500-0.5533-118	0.5533	0.5532	500	118	-	-	-	-
CSD-500-0.6238-118	0.6238	0.6236	500	118	-	-	-	-
CSD-500-0.6491-118	0.6491	0.6488	500	118	-	-	-	-
CSD-500-0.5533-250	0.5533	0.5530	500	250	-	-	-	-
CSD-500-0.6238-250	0.6238	0.6234	500	250	-	-	-	-
CSD-500-0.6491-250	0.6491	0.6450	500	250	-	-	-	-
CDCV-500-0.5533-118	0.5533	0.5532	500	-	118	-	-	-
CDCV-500-0.6238-118	0.6238	0.6236	500	-	118	-	-	-
CDCV-500-0.6491-118	0.6491	0.6488	500	-	118	-	-	-
CV-500-0.6238	0.6238	-	500	-	-	0.6238	5176.8	3586.6
CV-500-0.6280	0.6280	-	500	-	-	0.6280	4064.0	2795.6
CV-500-0.6312	0.6312	-	500	-	-	0.6312	2775.7	1893.2
CV-500-0.6381	0.6381	-	500	-	-	0.6381	32.11	22.10
CV-500-0.6438	0.6438	-	500	-	-	-	-	-
CV-500-0.6469	0.6469	-	500	-	-	-	-	-
CV-500-0.6491	0.6491	-	500	-	-	-	-	-
CV-500-0.6533	0.6533	-	500	-	-	-	-	-
CV-500-0.6585	0.6585	-	500	-	-	-	-	-
CV-500-0.6614	0.6614	-	500	-	-	-	-	-
CD-100-0.5928	0.5928	-	100	-	-	0.6369	128.7	86.77
CD-500-0.5533	0.5533	-	500	-	-	0.6304	659.1	477.3
CD-500-0.6059	0.6059	-	500	-	-	0.6325	656.03	468.06
CD-500-0.6142	0.6142	-	500	-	-	0.6341	1309.7	928.9
CD-2500-0.5781	0.5781	-	2500	-	-	0.6303	3232.7	2197.6
CD-5000-0.6482	0.6482	-	5000	-	-	0.6238	6477.7	4432.3